

Dynamics of laser-generated magnetic fields using long laser pulses

Hiroki Morita^{1,*}, Bradley B. Pollock,² Clement S. Goyon², Gerald J. Williams,² King Fai Farley Law^{1,3}, Shinsuke Fujioka^{1,†} and John D. Moody^{2,‡}

¹*Institute of Laser Engineering, Osaka University, 2-6 Yamada-Oka, Suita, Osaka 565-0871, Japan*

²*Lawrence Livermore National Laboratory, 7000 East Avenue, Livermore, California 94550, USA*

³*Department of Earth and Planetary Science, The University of Tokyo, 7-3-1 Hongo, Bunkyo-ku, Tokyo 113-0033, Japan*



(Received 13 July 2020; revised 25 October 2020; accepted 21 January 2021; published 1 March 2021)

We report on the experimental investigation of magnetic field generation with a half-loop gold sheet coil driven by long-duration (10 ns) and high-power (0.5 TW) laser pulses. The amplitude of the magnetic field was characterized experimentally using proton deflectometry. The field rises rapidly in the first 1 ns of laser irradiation, and then increases slowly and continuously up to 10 ns during further laser irradiation. The transient dynamics of current shape were investigated with a two-dimensional (2D) numerical simulation that included Ohmic heating of the coil and the resultant change of electrical resistivity determined by the coil material temperature. The numerical simulations show rapid heating at the coil edges by current initially localized at the edges. This current density then diffuses to the central part of the sheet coil in a way that depends both on normal current diffusion as well as temporal changes of the coil resistance induced by the Ohmic heating. The measured temporal evolution of the magnetic field is compared with a model that determines a solution to the coil current and voltage that is consistent with a plasma diode model of the drive region and a 2D simulation of current diffusion and dynamic resistance due to Ohmic heating in the laser coil.

DOI: [10.1103/PhysRevE.103.033201](https://doi.org/10.1103/PhysRevE.103.033201)

I. INTRODUCTION

Experimental study of magnetized plasma dynamics is an active area of research in the field of high-energy-density (HED) science. The generation of strong magnetic fields has been developed at several facilities and is being applied to HED experiments. There are several techniques for generating a strong magnetic field. For example, nondestructive single-turn and Helmholtz coils driven by pulsed-power devices are typically used to generate magnetic fields below ~ 100 T for a long time (>1 μ s) and large scale (>1 mm³) [1–4]. These coils have been successfully used in astrophysical HED experiments such as the formation of plasma jets [5,6] and shocks [7,8]. Above 100 T these coils explode and emit debris, which can put diagnostics and laser optics at risk. A laser-driven coil does not require a separate pulsed power system, and it has been shown in a number of experiments to produce $B \geq 100$ T at high-power laser facilities such as GEKKO-XII [9,10], OMEGA-EP [11,12], LULI2000 [13,14], and Shenguang-II [15]. The temporal and spatial scales of the magnetic field generated by the laser-driven coil tend to be shorter time (~ 1 ns) and smaller volume (~ 1 mm³) compared to the conventional devices. However, the laser-driven coil itself is small and has less debris generation. Thus, it can be easily implemented in laser-based HED experiments and is good for the maintenance of a laser laboratory composed of expensive optical elements. Because of these advantages, the laser-driven coils have been used and are planned to be used in numerous

HED experiments such as those on magnetic reconnection [16], magnetohydrodynamic instability [17], charged-particle beam control [18–20], laser-plasma interactions [21–23], and inertial confinement fusion [24–27]. Despite the significant number of HED studies performed with laser-driven coils, the mechanism of magnetic field generation is still not fully understood.

A widely used laser-driven coil consists of two plates and one loop-coil connecting the plates. The plates supply voltage, and a magnetic field is generated by the current flowing in the coil. The laser-driven coil was first demonstrated by Korobkin and Motylev using a 1054-nm laser [28]. Seely *et al.* [29] and Daido *et al.* [30] improved the understanding of this coil. Courtois *et al.* proposed a model based on a lumped-element RLC circuit [31]. In their model, a laser generates a space-charge current between two plates, which charges the two-plate capacitor to a voltage that corresponds to a few times the temperature of the nonthermal hot electrons generated by the laser drive. The voltage on this capacitor then drives a current through the coil. The current begins to decay even during the laser-irradiation once the accelerated ion front crosses the gap between the two plates and reaches the cathode plate. The timescale for this decay is d/C_s , where d and C_s are the separation distance between the plates and the sound speed of the plasma, respectively. This model was modified by Goyon *et al.* to include the self-consistent charging of the plate capacitor, the space-charge current generated by the hot electrons, and the temporal evolution of the capacitance due to Debye shielding by the plasma between the two plates [13]. Fiksel *et al.* [32] proposed a model based on a lumped-element RLC circuit that considers thermal electron and ion currents in addition to the nonthermal hot-electron current.

*morita-h@ile.osaka-u.ac.jp

†sfujioka@ile.osaka-u.ac.jp

‡moody4@llnl.gov

This model gives a lower magnetic field amplitude compared to that observed in experiments.

Tikhonchuck *et al.* developed a laser-driven diode model [33] that predicts the magnetic field remains during the laser-pulse, unlike the prediction by the above models. In this model, the plasma initially exhibits one-dimensional planar expansion from the laser-irradiated plate as described by Mora [34]. The planar expansion transitions to a spherical expansion after the expansion front travels a distance equal to the laser spot radius. This spherical expansion is stationary in time and generates a plateau potential distribution in the gap. This potential remains during the laser irradiation, allowing the current to keep flowing. The current, i.e., electron flow, is limited by the potential distribution (space-charge limit) and by the self-generated magnetic field (self-magnetization limit) that is similar to the Alfvén limitation mechanism. These two mechanisms of the electron current limit are considered in this model. This model also considered the change of coil resistance and the modification of the coil geometry due to Ohmic heating. The model explains fairly well several experiments obtained at different laser facilities using a laser intensity of $>1 \times 10^{15}$ W/cm² and a pulse duration of ~ 1 ns. Recently, the laser-driven diode model was experimentally tested at a low laser intensity ($\leq 10^{14}$ W/cm²) and a pulse duration ranging from 0.5 to 20 ns [35]. In this experiment, the generated voltage and current were measured directly. The results showed that the voltage and current are retained during the laser irradiation. These results can be explained by assuming that the laser drive creates a voltage source that is approximately equal to the laser-heated electron temperature, $k_B T_e$. The relatively small (< 100 A) current means that the Ohmic heating effect on coil resistance was negligible. The behavior of the laser-generated magnetic field in the transition from a single-temperature thermal electron energy distribution to a nonthermal hot-electron component has not been explored because there is little to no hot-electron component for this low-intensity laser drive.

The motivation of our study is to generate a magnetic field of > 100 T lasting up to 10 ns by using a 10-ns and 0.5-TW high-power laser. In this paper, we show the experimental results for laser-generated magnetic fields with long-duration (10 ns) and high-power (0.5 TW) laser pulses, and we present an advanced theoretical model of the laser-driven magnetic field that includes current dynamics by the laser-drive, current diffusion, and Ohmic heating all self-consistently. We discovered that a laser-driven coil can maintain a magnetic field of a few hundred tesla during the laser pulse duration (at least 10 ns and possibly much longer) even after low-density plasma fills the vacuum gap between the plates. During laser irradiation, the magnetic field strength increases gradually after ramping up quickly. Further, our numerical simulations are done for the duration of the experiment and show spatial and temporal changes of the magnetic field topology. We attribute these changes to transient current diffusion and Ohmic heating induced by the dynamic evolution of current density in the coil. We show that the experimental results can be reproduced with a theoretical model that accounts for the laser drive, the current diffusion, and the temporal evolution of the resistance of the half-loop sheet coil. This is a useful result for HED experiments; an extension of the magnetic field pulse longer

than 1 ns is required for the investigation of the magnetized HED plasma dynamics, which generally takes place in a nanosecond timescale, e.g., magnetized inertial confinement fusion and collisionless shock experiments. For these HED experiments, the laser-driven coil has to drive a current even with sample materials inside a loop during the pulse. This should be investigated in future experiments.

II. EXPERIMENTAL SETUP

The experiments were conducted at the OMEGA-EP facility. Figure 1 shows the experimental setup. One of two OMEGA-EP beams, whose pulse shape is square (100-ps rise time) and duration is 10 ns, passes through holes on the front plate and irradiates the back plate of a half-loop gold sheet coil with a 25-degree off-normal incidence angle. The laser energy, intensity, and wavelength are 5 kJ, 2.2×10^{15} W/cm², and 351 nm, respectively. The surface of the back plate is coated with a 10- μ m-thick plastic layer to increase the plasma scale length, resulting in higher-energy electron generation via laser-plasma interactions. The radius, thickness, and width of the half-loop sheet coil are 250 μ m, 12.5 μ m, and 1.15 mm, respectively.

In our experiment, the coil has three through holes on the front plate and three exit slots on the back plate, which allow the field amplitude to be observed at three points along the central axis of the coil. A previous experiment using a similar target [13] quantified the magnetic field strength at the center of the coil; however, the target had only one hole-slot pair for proton deflectometry. The front side faces the proton source. Protons passing through the holes are deflected downward by the magnetic field in the coil. The deflected protons exit through the slots toward the detector. The wide sheet coil used in this experiment is unlike the thin-wire coils used in other laser-driven magnetic field studies. The wide coil enhances the current diffusion effects and nonuniform Ohmic heating in the magnetic field generation process, which are not observed clearly in a thin-wire coil. The initial circuit parameters for the coil, which are calculated based on the geometry and tabulated normal gold properties, are $R = 5.4$ m Ω , $L = 0.4$ nH, and $C = 0.06$ pF.

Proton deflectometry is the primary method used to measure the amplitude of the magnetic field in this experiment. A 1-ps 1054-nm pulse with an intensity of 8×10^{18} W/cm² is focused onto 10- μ m-thick gold foil to generate protons that range from a few to 30 MeV of energy via the target normal sheath acceleration mechanism [36,37]. The proton source is placed 6.5 mm from the laser-driven coil. Deflected protons are detected using radiochromic film (RCF) stacks located 80 mm from the coil. A stack of eight RCFs is used to detect protons up to 29.4 MeV [38]. A copper screen with a 65- μ m wire spacing in a square grid is used to track the deflection of protons across the entire image.

III. ANALYSIS METHOD

Figure 2 shows the experimental (right half) and simulated (left half) proton images in the case of (a) no laser-irradiation and images obtained at (b) 0.62, (c) 1.15, and (d) 7.08 ns after the beginning of the laser irradiation, respectively. The

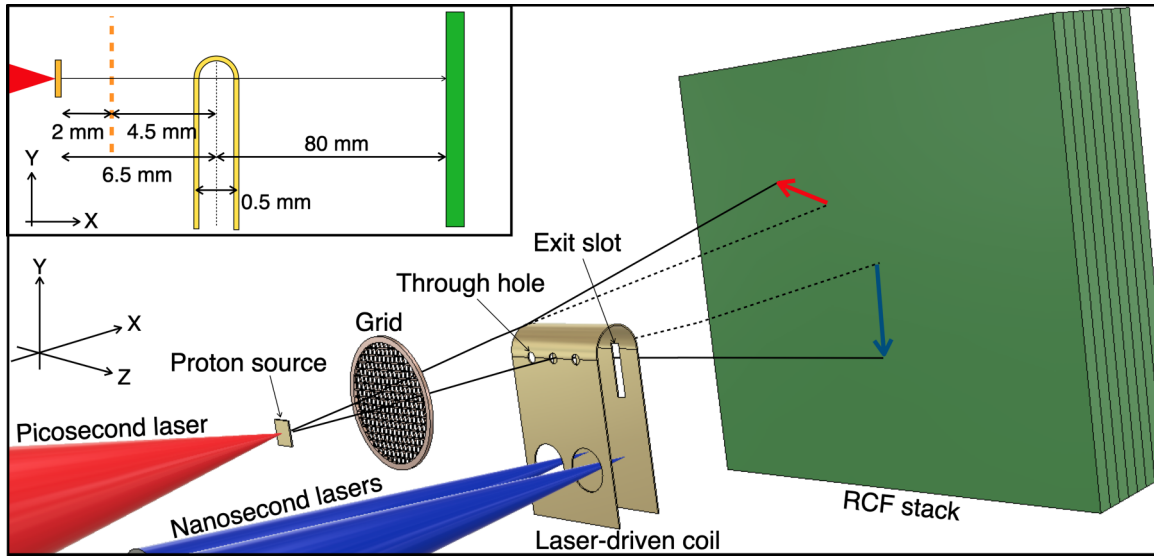


FIG. 1. Experimental setup of proton deflectometry for the measurement of the magnetic field which is illustrated in three and two dimensions. The magnetic field is generated with a half-loop gold sheet coil driven by one of two nanosecond OMEGA-EP beams that have an energy of 5 kJ, a power of 0.5 TW, and a duration of 10 ns. The generated magnetic field is toward the z -direction. The protons are generated from the thin gold foil irradiated with a picosecond OMEGA-EP beam, which have an intensity of 8×10^{18} W/cm². The proton beam imprint by the grid is deflected by the generated magnetic field and detected by radiochromic films.

time origin is defined at the half-maximum of the rising edge of the coil-driving laser pulse. The protons detected by the RCF layer shown in Figs. 2(c) and 2(d) have an energy of 29.4 MeV.

The magnetic field strength is estimated from the proton deflection pattern and then compared to that in simulated proton images, as shown in Fig. 2. The field amplitude at the edges of the coil (defined as the edge magnetic field) can be inferred from the width of the proton shadow indicated by the red arrow. Measurement of the proton shadow width can provide the time evolution of the edge magnetic field for a long time duration. The protons are primarily subjected to the fringing magnetic field around the coil. Here, we estimated the edge magnetic field by matching the width (edge to edge length) of the simulated proton image to the experimental image. In this analysis, the current density in the target was unknown from the experiment, thus we used two limiting cases to estimate the edge magnetic field: a uniform current density and an edge-peaked current density.

The uncertainty in the edge magnetic field is caused by three sources: proton energy resolution corresponding to an RCF layer, the uncertainty in current density distribution (uniform or edge peaked), and scattering of protons by plasma and the coil itself. The errors in the width are estimated by fitting both edges using a Gaussian error function given as

$$y = \frac{a}{2} \left[1 \pm \operatorname{erf} \left((x - x_0) \times \frac{2\sqrt{\ln 2}}{\delta} \right) \right] + y_0, \quad (1)$$

where a , x_0 , and y_0 are fitting parameters, and y corresponds to signal intensity on an RCF. The full width at half-maximum of the Gaussian function, δ , corresponds to the error of the width. This error automatically includes the energy resolution corresponding to an RCF layer, the scattering effect by surrounding plasma, and the coil. The widths of the proton shadows were converted to magnetic field strengths with a formula relating the shadow width and the magnetic field strength. The errors due to the uncertainty of the current density distribution appear in the magnetic field through this conversion.

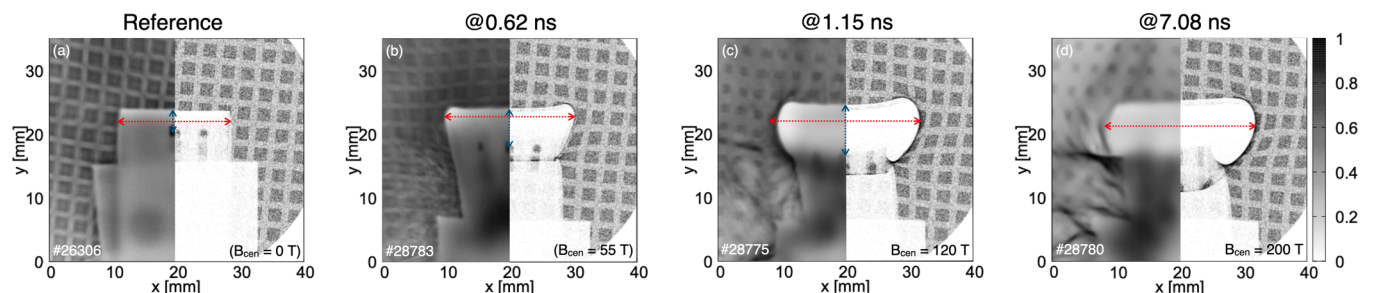


FIG. 2. Comparisons between the experimental (right half) and computed (left half) proton images in the case of (a) no laser-irradiation (cold target) and images obtained at (b) 0.62, (c) 1.15, and (d) 7.08 ns after the beginning of the laser irradiation. The computed image reproduces well the experimental proton image. The small difference in the shape of the coil shadow between left and right comes from the difference in coil shape, namely a half-loop in the experiment and a cylinder in the calculation.

The temporal evolution of the estimated magnetic field is discussed in Sec. VI. The magnetic field at the three holes can be estimated from the vertical shifts of the proton dots indicated by the blue arrow. The vertical shift of the dots corresponds to the integral of the Lorentz force along the full trajectory of the protons. The proton dots corresponding to the three through holes can be clearly seen at relatively early times, as shown in Figs. 2(b) and 2(c). However, the proton dots become quite weak at later times, as shown in Fig. 2(d). This occurs because the protons are deflected so much downward and possibly with a slight asymmetric deflection to the side that they cannot escape from the inside of the coil region through the exit slots. A particle transport simulation shows that scattering and stopping of protons in the plasma filled between the plates are negligibly small in this measurement. We can place a lower bound on the magnetic field amplitude at these axial locations; however, the uncertainty in these data makes this unsuitable for precisely quantifying the magnetic field and, as we discuss later, the local current density due to the current diffusion in the central coil region. Future experiments should extend the holes further downward and widen them to accommodate larger proton shifts in both directions and obtain a better signal from the through holes.

The right-half images of Figs. 2(a)–2(d) show computed proton images obtained using 2D (r and z) cylindrically symmetric magnetic fields instead of the actual half-loop geometry. The proton image shown in Fig. 2(a) corresponds to a cold reference of the proton deflection which is calculated without any magnetic fields. The right proton images shown in Figs. 2(b) and 2(c) were calculated with the edge-peaked current distribution, where the strengths of a magnetic field at the center of the coil are set to be 55 T for (b) and 120 T for (c). The right proton image in Fig. 2(d) was calculated with the uniform current distribution, where the magnetic field is set to be 200 T at the center of the coil. These computed images (right-half) reproduce well the experimental proton image (left-half). The small difference in the shape of the coil shadow between experimental and simulation results comes from the difference in a coil shape, namely a half-loop in the experiment and a cylinder in the calculation. The proton beam pattern became worse at later timings because the TNSA source was preheated by radiation from the coil itself. This simplified 2D geometry is a good surrogate for the experimental coil geometry (half-cylinder attached to two plates) and is estimated to have current diffusion timescales similar to those in the experiment. The cylinder geometry is also more easily modeled and can provide useful insight for understanding the experimental results. The geometrical error for the edge field between the 2D cylinder and the three-dimensional half-loop coil is less than 1% [13]. The simulation uses a Monte Carlo method with 10^6 particles to generate the proton images through a magnetic field table; this was calculated from a prescribed current density in the coil.

IV. CURRENT DIFFUSION AND OHMIC HEATING

The current diffusion along only the axial direction was considered in the evaluation of the diffusion time in previously reported OMEGA-EP laser-driven coil experiments. The diffusion time was calculated with a one-dimensional

diffusion model for a conductor [39]. The axial diffusion time is much longer (> 1000 ns) than the laser pulse (1 ns), and thus static current and magnetic distributions were assumed in the previous analysis. However, simple estimates show that the radial current diffusion time is approximately $4\mu_0\sigma d^2/\pi^2 = 3.2$ ns, which is much shorter than the axial diffusion time and pulse duration (10 ns) in our experiment, where σ is the electrical conductivity of gold (the common reference value is 4.09×10^7 S/m at 300 K). Thus, the current diffusion dynamics must be considered here.

In addition to the current diffusion, the large current (~ 100 kA) resistively heats the gold coil, leading to a temporal change in coil resistivity, as described in a previous study [40]. Note that current diffusion is typically a linear process, but it becomes nonlinear in cases with significant Ohmic heating [40,41]. The current redistribution resulting from these effects allows a significant current density to flow in the entire coil region even at an early time in the laser pulse. The current diffusion also affects the total resistance $R(t)$, changing the time evolution of the current density and the generated magnetic field. In this section, we show the results of a simulation that models current diffusion and the material temperature change from Ohmic heating.

We investigated the effects of current diffusion and Ohmic heating using a 2D cylindrical transient simulation [42]. This 2D simulation does not model the gap in the target cylinder where the plates attach and does not include the plates, as was done by Goyon [13]. The most important effects we included here are the radial and axial current diffusion and the Ohmic heating effects on current density. These effects can be well modeled in two dimensions.

The modeled cylinder is pure gold, with an inner radius of $a = 250$ μm , a thickness of 12.5 μm , and a length of 1.15 mm. This matches the dimensions of the half-loop coil used in the experiments. Null current and room temperature are set as the initial conditions. In the laser-driven coil, the voltage is supplied by the laser drive between the two flat plates. We implemented this voltage by imposing a slowly time-varying electric field defined as $E_{\text{back},\phi}(r, z, t) = E_0(t)r/a$ throughout the solution volume. The total electric field is expressed as $\vec{E} = \vec{E}_{\text{back}} + \vec{E}_{\text{ind}}$, where \vec{E}_{ind} is the electric field that results from the time changing magnetic field. Note that the background electric field vanishes at $r = 0$ and is used to drive the current in the conductor. Similarly, the total magnetic field is expressed as $\vec{B} = \vec{B}_{\text{back}} + \vec{B}_{\text{ind}}$. The time-varying part $E_0(t)$ is determined by iterating to a consistent solution between the numerical simulation and the circuit model that we describe in the next section. This background electric field generates a spatially uniform background magnetic field such that $B_{\text{back},z}(t) = -\int_0^t dt' [\vec{\nabla} \times \vec{E}_{\text{back}}(t')]_z = -\int_0^t dt' 2E_0(t')/a$. Here, we focus on the magnetic field generated by the current in the cylinder, and thus we subtract the background magnetic field from the calculated magnetic field. In this transient simulation, the electric and magnetic fields are numerically calculated from the following Maxwell's equations:

$$\frac{\partial \vec{E}_{\text{ind}}}{\partial t} = \frac{1}{\mu\epsilon} \vec{\nabla} \times \vec{B}_{\text{ind}} - \frac{\sigma}{\epsilon} (\vec{E}_{\text{back}} + \vec{E}_{\text{ind}}) - \frac{\partial \vec{E}_{\text{back}}}{\partial t}, \quad (2)$$

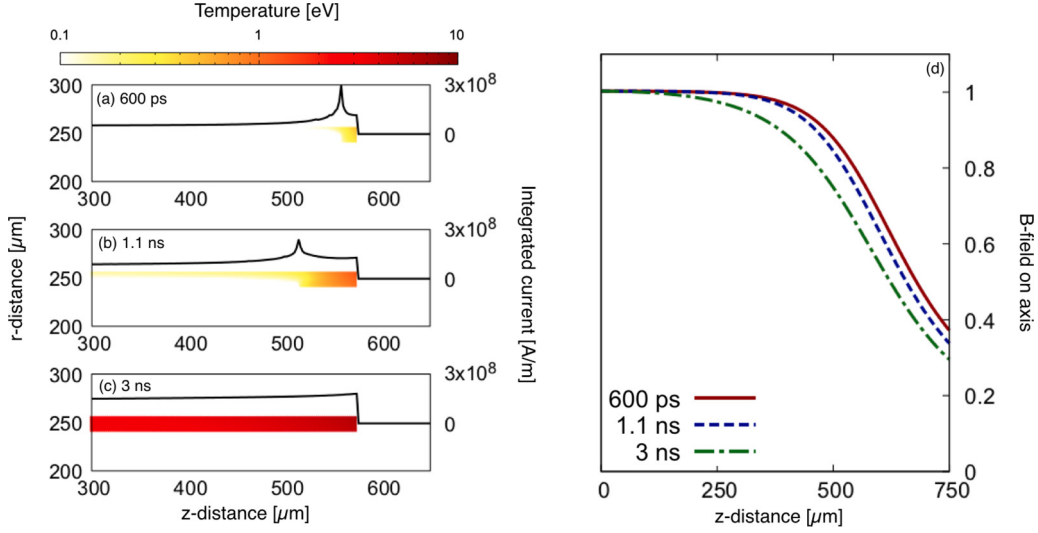


FIG. 3. Line-outs of the integrated current density and 2D distribution of the coil temperature at (a) 0.6 ns, (b) 1.1 ns, and (c) 3 ns after laser irradiation from the transient simulation. We also plot in (d) a line-out of the magnetic field distribution along the central axis. The integrated current density approaches a uniform distribution accompanied by current diffusion and heating from the edges to the whole body. The width of the magnetic field narrows because of the current density diffusion. The magnetic fields are normalized by the value at the center.

$$\frac{\partial \vec{B}_{\text{ind}}}{\partial t} = -\vec{\nabla} \times (\vec{E}_{\text{ind}} + \vec{E}_{\text{back}}) - \frac{\partial \vec{B}_{\text{back}}}{\partial t} = -\vec{\nabla} \times \vec{E}_{\text{ind}}. \quad (3)$$

The induced electric and magnetic fields were solved over a whole solution volume with the applied background electric field. Ohmic heating is included as $c_V \rho \partial T / \partial t = \sigma(T) |E_\phi + E_{\text{back},\phi}|^2$, where c_V and ρ are the isochoric specific heat and density of gold, respectively. Thermal diffusion is too small to matter at the experimental timescale. The detailed description was discussed in Ref. [42]. Simulations were run in a $1000 \mu\text{m} \times 2000 \mu\text{m}$ calculation boundary with a $2\text{-}\mu\text{m}$ mesh size.

The simulation used the conductivity table of gold produced with *ab initio* calculations [43]. Here, we assumed an isochoric Ohmic heating process during the pulse. The conductivity of gold decreases with temperature in the solid phase. As the temperature approaches 1 eV, gold transitions to the warm-dense-matter phase and the conductivity tends to be a constant value of about 10^6 S/m . At higher temperature (i.e., in the plasma phase), the conductivity begins to increase. We will discuss the details in a separate work.

Figures 3(a)–3(c) show line-outs of the current density integrated in the radial direction and 2D distributions of the coil temperature at times of (a) 0.6 ns, (b) 1.1 ns, and (c) 3 ns. At 0.6 ns, the simulated current density has a strong peak at the edges of the coil. This current rapidly heats the coil edges, which decreases both the conductivity and current in this region. Because the central region of the coil is still at room temperature and has high conductivity, the peak of the current density shifts inward to the cold central coil region, as shown by the line-out for 1.1 ns. In addition to the conductivity change caused by Ohmic heating, the radial current diffusion contributes to the redistribution of the current density, as shown in the line-outs for 1.1 and 3 ns. At 3 ns, the entire coil is heated and the fine structure of the current density is smoothed to a roughly spatially uniform value. At

still later time, the current gradually increases as the entire coil heats and the conductivity increases. Figure 3(d) plots the magnetic field amplitude at the three times normalized by the value at the coil center. The magnetic field on the axis spreads widely due to the edge-peaked structure of the current density at 0.6 ns. As the current diffuses, the width of the magnetic field narrows due to the shift of the current peak and the increase in current flow in the inner part. Later, the width of the magnetic field becomes narrower because the current density distribution approaches the uniform distribution. However, the edge magnetic field shows a fairly weak sensitivity to the spatial distribution of current. We conclude that it would be difficult to experimentally verify current diffusion from only a measurement of the spatial dependence of the edge magnetic field in this geometry. Rather, accurate measurements of the field in the center region of the coil are needed.

The transient simulation can be used to estimate a time-dependent resistance, which is needed to form an accurate circuit model of the laser coil. In the next section, we discuss how we model the temporal evolution of the coil current and include the time-dependence resistance.

V. LASER-DRIVEN DIODE MODEL

If the plates supply a voltage $V(t)$, simple lumped-circuit equations for the coil current are given by

$$C(t) \frac{dV}{dt}(t) = I_d(t) - I(t), \quad (4)$$

$$V(t) = L(t) \frac{dI}{dt}(t) + I(t)R(t), \quad (5)$$

where $L(t)$ is the coil inductance and $R(t)$ is the time-dependent coil resistance. Equation (4) is important only for creation of the supplied voltage at early time. Note that if the capacitance, $C(t)$, is small, we can reduce the equations to only Eq. (5) because the coil current becomes equivalent to the drive current, $I_d(t)$, which is described later. The capacitance

in this experiment is small, thus we used only Eq. (5) to calculate the temporal evolution of $I(t)$ and $V(t)$.

The coil inductance initially determines the rate of current increase; therefore, the current in the coil starts out small even though a large voltage is applied to the coil in the start-up phase. As the current in the circuit increases, it is limited by one of two possible mechanisms that are active in the laser drive region: (i) space-charge limitation or (ii) self-magnetization limitation. The plasma diode model [33] provides a description of the conditions that cause the two current limitations.

Throughout the laser drive, the voltage-current relation in the space-charge-limited region is given by

$$I = I_0 e^{-eV/k_B T_{\text{hot}}}. \quad (6)$$

The quantity I_0 is the maximum possible current for a given laser intensity and is defined as $I_0 = en_h \pi r_L^2 v_h$, where r_L , n_h , and v_h are the laser focal radius, the hot electron density, and the hot electron velocity, respectively, which give an I_0 value of 50 MA for our condition. As the current through the coil increases, the voltage decreases according to Eq. (6). This limit does not include the normal energy distribution of hot electrons, and thus the current limit at low $eV/k_B T_{\text{hot}}$ is overestimated. Including a Maxwellian energy distribution for the hot electrons gives the following modified space-charge current limit equation:

$$I = I_c (1 + eV/k_B T_{\text{hot}}) e^{-eV/k_B T_{\text{hot}}}, \quad (7)$$

where I_c is the maximum current proposed by Courtois [31], defined as $I_c = ehI_L \pi r_L^2 / (2T_{\text{hot}})$. The values I_L and h are the laser intensity and the conversion rate from the laser to hot electrons, respectively. We find from our analysis that the conversion rate of $h = 0.1$ shows good agreement with our experimental results.

The self-magnetization limit is caused by the prohibition of a large current by the self-generated magnetic field. The maximum current and voltage relation in this case is given by [44] $I_m = V/Z_D$, where

$$Z_D = \sqrt{\frac{\mu_0}{2\epsilon_0}} \frac{\lambda_h}{\pi \alpha r_L}. \quad (8)$$

In this formula, λ_h is the Debye length for hot electrons. The parameter α is a geometrical factor (maximum value = 1) that corresponds to the divergence angle of hot electrons that emit from the back plate. We estimate the hot electron temperature in our experiment to be 7 keV [45], giving an effective impedance of $Z_D = 0.034 \Omega$ using $\lambda_h = 3.2 \times 10^{-6} \text{ m}$ and $\alpha = 1$. The number density of hot electrons is calculated as

$$\frac{n_h}{n_c} = 0.2 \left(\frac{I_L \lambda_L^2}{T_{\text{th}}} \right) \quad (9)$$

assuming 5.7 keV for the thermal electron temperature [46]. Here, n_c and λ_L are the critical density and wavelength of the incident laser, respectively. The maximum current possible in the coil is obtained by setting $\alpha = 1$ and substituting $V = I_m Z_D$ in Eq. (7). Solving for the maximum current gives $I_{\text{max}} = 680 \text{ kA}$ and $V = 21 \text{ kV}$. This is the maximum current that would flow in the drive region if the two capacitor plates were shorted with no additional impedance.

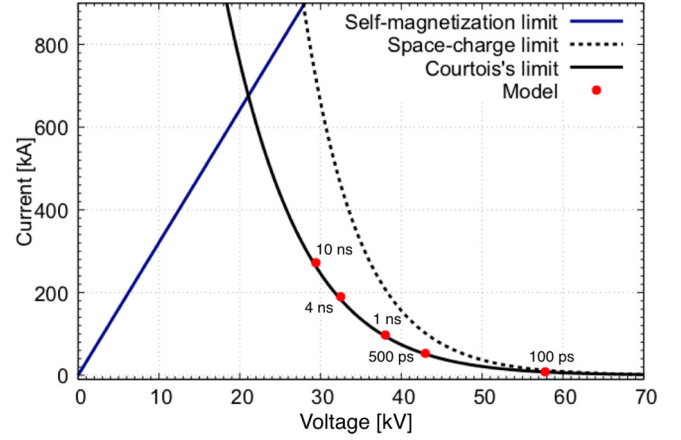


FIG. 4. Relation between voltage and current (V - I) based on the laser-diode model. The current in a laser-driven coil is limited by the space-charge potential (solid and dashed black lines) and the self-magnetization of hot electron flow (blue line). The maximum current is limited to 680 kA at 21 kV. The red points show the temporal change of the V - I relation in this experiment. The calculated current is mainly limited by the space-charge potential labeled as Courtois's limit.

Figure 4 shows the Courtois space-charge limited V - I relation Eq. (7) for this experiment in solid black. The dotted black curve is the simple space-charge limited V - I relation Eq. (6). The blue line shows the magnetization limit. Figure 4 also plots the V - I relation solved using the self-consistent iteration method as red points. It can be seen easily now that the calculated circuit current and supplied voltage are located in the Courtois's space-charge-limited region. Note that at 10 ns, the experiment is still on the space-charge-limited curve. Thus, space-charge is the dominant mechanism that limits the current in the drive region and in the circuit for our experimental conditions.

We wish to find a self-consistent solution for the circuit voltage, current, and resistance in Eqs. (5) and (7) that is also consistent with the numerical solution to the cylindrical simulation that accounts for current diffusion and coil heating. Here we developed an iterative method that starts with a time-constant voltage applied to the cylinder simulation. From this constant voltage, we obtain a current density, $j_\phi(r, z, t)$, and a magnetic field, $\vec{B}(r, z, t)$, in the cylinder that we use to determine the total current, $I(t)$, the effective resistance, $R(t)$, and inductance, $L(t)$, that can be used in Eq. (1). The total current, $I(t)$, can be obtained by integrating $j_\phi(r, z, t)$ over the cross-section. The time-dependent resistance and inductance for the cylinder coil can be calculated from the transient simulation with following relations:

$$R_{\text{cyl}}(t) = \int_{\text{coil}} dV \sigma(T) |E_\phi(r, z, t)|^2 / I(t)^2 \quad (10)$$

and

$$L_{\text{cyl}}(t) = \frac{1}{\mu_0} \int dV |\vec{B}(r, z, t)|^2 / I(t)^2. \quad (11)$$

Consequently, we can estimate the time-dependent resistance for the actual half-loop coil, $R(t)$, using the relation $R(t) = R_{\text{cyl}}(t) \times l_U / l_{\text{cyl}}$, where the geometrical factor l_U / l_{cyl} is

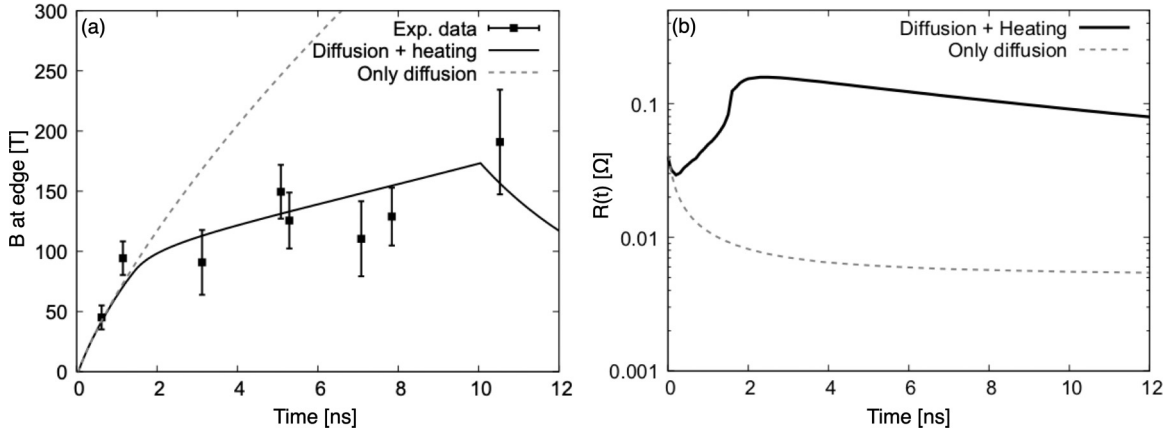


FIG. 5. Time evolution of (a) the edge magnetic field estimated from the experiment (filled squares) and calculated using the circuit model (solid black curve), and (b) the effective resistance calculated with the 2D transient simulation. We also show the predicted magnetic field resulting from including only the current diffusion (resistivity is temperature-independent). The circuit model with the time-dependent resistance estimated from the transient simulation has good agreement with the experimental data.

calculated to be $3.71 \text{ mm}/1.57 \text{ mm} = 2.36$. For the inductance, we use a constant value of 0.4 nH in the model calculation because we find that the temporal change of the inductance estimated by Eq. (7) is negligibly small ($<0.01 \text{ nH}$), and will not affect the temporal evolution of $I(t)$ much. Now that we have $R(t)$, which includes current diffusion and Ohmic heating, we can solve Eq. (5) for the current time history in the half-loop coil. Continuing to the second iteration, we now obtain a new voltage $V(t)$ from Eq. (1). This voltage, $V(t)$, is converted to the cylinder voltage for use in the simulation using the relation $V_{\text{cyl}}(t) = V(t) \times l_{\text{cyl}}/l_U$ [corresponding to $E_0(t) = V(t)/l_U$]. This $V_{\text{cyl}}(t)$ is now used in the cylinder simulation to solve for the new $R(t)$. Iterating this loop until $V(t)$, $I(t)$, and $R(t)$ converge well between iterations, and it yields the self-consistent solution, which includes space-charge-limited current flow, circuit inductance, current diffusion, and Ohmic heating. We note that using the geometrical scaling between the cylinder and the actual half-loop coil, where we multiply $V(t)$ and $R(t)$ by a factor l_{cyl}/l_U , gives the same Ohmic heating per unit mass for the cylinder and coil target.

VI. TEMPORAL EVOLUTION OF MAGNETIC FIELD

We finally consider the temporal evolution of the magnetic field for times up to 10 ns. Figure 5(a) shows the edge magnetic field (filled squares) evaluated from the measurements and the modeled magnetic field time history, which includes current diffusion and Ohmic heating (solid black). Here the edge magnetic field means the field amplitude at the edges of the coil. One can see that the estimated magnetic field increases rapidly during the first 1 ns. This rapid turn-on of the field has also been observed in 1-ns pulses [13] and low-power laser experiments [35]. The field after 1 ns shows a slower increase until the end of the laser drive. Based on our analysis, we explain the gradual increase in the magnetic field between 1 and 10 ns as the result of the coil resistance decreasing due to the Ohmic heating. The lower resistance leads to a longer L/R time constant, causing the gradual increase in the magnetic field.

The modeled magnetic field strengths (solid black) show good agreement with the measured value. The temporal behavior of the field after laser shut-off at 10 ns was not investigated in these experiments. Nevertheless, we estimated the magnetic field time dependence after laser shut-off shown in Fig. 5(a) using the expected L/R decay of the current in the target and neglecting any capacitive effects. Based on the work of Goyon *et al.* [13] and Williams *et al.* [35], we acknowledge that the magnetic field time dependence after laser shut-off is more complex than this because there is likely a capacitive effect from the front and rear target plates. The details of this effect require further measurements before it can be included in our model.

Figure 5(a) also plots the modeled magnetic field considering only the current diffusion, i.e., where we assume the resistivity is independent of material temperature (dashed gray). In this case, the coil resistance just decreases due to the current diffusion, and the resulting magnetic field (and total current) increases. This result does not match the experimental data, and it shows the importance of including the effects of Ohmic heating. Note that the edge magnetic field amplitude was estimated from the diode model using the formula $B_{\text{edge}} = 0.6 \times I$ within $\pm 10\%$ error, which was obtained from the results of the transient simulation.

Figure 5(b) shows the temporal evolution of the scaled time-dependent resistance, which is calculated from our transient simulation by considering current diffusion and Ohmic heating (solid black), and only the current diffusion (dashed gray). At the beginning ($<100 \text{ ps}$), both resistances decrease due to the current diffusion. If only the current diffusion takes place, the resistance continues decreasing and converges to $5.4 \text{ m}\Omega$. However, the conductor is heated enough to significantly change the resistivity in this experiment. As a result, the increase in resistance due to heating is faster than the resistance decrease due to the diffusion. The coil conductor begins to melt around 1.6 ns, causing its resistance to jump to $0.15 \text{ }\Omega$. After melting, the coil resistance slowly decreases due to continued Ohmic heating. This slow decrease of the resistance causes the gradual increase of the modeled magnetic field.

VII. SUMMARY

In summary, we show the measurements of a laser-generated magnetic field with a long-duration (10 ns) and high-power (0.5 TW) laser pulse. The results of proton deflectometry measured at different timings indicate that the magnetic field rises rapidly in ~ 1 ns and then increases slowly for the remainder of the laser pulse. The laser-driven diode model coupled with the simulation of Ohmic heating and current diffusion shows good agreement with the experimental data. These are the results of modeling the laser-driven coil with an iterative solution method that includes dynamic resistance, current diffusion, and space-charge current limitation self-consistently. The dynamics of current diffusion and Ohmic heating are simulated with a 2D transient model using cylindrical geometry. The simulation results show that the localized current at the coil edges heats the edges immediately, causing the current density to shift inward as a result of reduced conductivity by Ohmic heating.

The central deflection of the proton beam could not be accurately measured at later times in this experiment because the protons could not escape through the exit slots on the coil. We recommend that in future experiments the exit slots should be made large enough to accommodate the significant

vertical and horizontal deflections of the protons. Future experiments with larger exit slots will be able to characterize the evolving magnetic field topology and draw conclusions about the dynamics of current diffusion experimentally with the through-hole method.

ACKNOWLEDGMENTS

The authors thank the technical support staff of the Laboratory for Laser Energetics at the University of Rochester for assistance with OMEGA-EP. The authors appreciate greatly valuable discussions with V. Tikhonchuk (CELIA). This work was performed under the auspices of the US Department of Energy by Lawrence Livermore National Laboratory under Contract No. DE-AC52-07NA27344. This work was partially supported by Japan/U.S. Cooperation in Fusion Research and Development, the Collaboration Research Program between the National Institute for Fusion Science and the Institute of Laser Engineering at Osaka University, and the Osaka University Scholarship for Overseas Research Activities 2018, KAKENHI (Grants No. 15KK0163, No. 16K13918, and No. 16H02245), the Matsuo Research Foundation, and the Research Foundation for Opto-Science and Technology.

-
- [1] O. Portugall, N. Puhlmann, H. U. Muller, M. Barczewski, I. Stolpe, and M. Ortenberg, Megagauss magnetic field generation in single-turn coils: New frontiers for scientific experiments, *J. Phys. D* **32**, 2354 (1999).
- [2] B. Albertazzi, J. Beard, A. Ciardi, T. Vinci, J. Albrecht, J. Billette, T. Burris-Mog, S. N. Chen, D. DaSilva, S. Dittrich, T. Herrmannsdorfer, B. Hirardin, F. Kroll, M. Nakatsutsumi, S. Nitsche, C. Riconda, L. Romagnani, H.-P. Schlenvoigt, S. Simond, S. Veuillot, T. E. Cowan, O. Portugall, H. Pepin, and J. Fuchs, Production of large volume, strongly magnetized laser-produced plasmas by use of pulsed external magnetic fields, *Rev. Sci. Instrum.* **84**, 043505 (2013).
- [3] R. V. Shapovalov, G. Brent, R. Moshier, M. Shoup, R. B. Spielman, and P.-A. Gourdain, Design of 30-T pulsed magnetic field generator for magnetized high-energy-density plasma experiments, *Phys. Rev. Accel. Beams* **22**, 080401 (2019).
- [4] P. Hu, C. Y. Wang, H. B. Tang, Z. C. Zhang, and J. Zheng, Pulsed magnetic field device for laser plasma experiments at Shenguang-II laser facility, *Rev. Sci. Instrum.* **91**, 014703 (2020).
- [5] B. Albertazzi, A. Ciardi, M. Nakatsutsumi, T. Vinci, J. Beard, R. Bontio, J. Billette, M. Borghesi, Z. Burkley, S. N. Chen, T. E. Cowan, T. Herrmannsdorfer, D. P. Higginson, F. Kroll, S. A. Pikuz, K. Naughton, L. Romagnani, C. Riconda, G. Revet, R. Riquier, H.-P. Schlenvoigt, I. Y. Skobelev, A. Y. Faenov, A. Soloviev, M. Huarte-Espinosa, A. Frank, O. Portugall, H. Pepin, and J. Fuchs, Laboratory formation of a scaled protostellar jet by coaligned poloidal magnetic field, *Science* **346**, 6207 (2014).
- [6] T. Byvank, J. T. Banasek, M. Potter, J. B. Greenly, C. E. Seyler, and B. R. Kusse, Applied axial magnetic field effects on laboratory plasma jets: Density hollowing, field compression, and azimuthal rotation, *Phys. Plasmas* **24**, 122701 (2017).
- [7] D. B. Schaeffer, W. Fox, D. Haberberger, G. Fiksel, A. Bhattacharjee, D. H. Barnak, S. X. Hu, K. Germaschewski, and R. K. Follett, High-Mach number, laser-driven magnetized collisionless shocks, *Phys. Plasmas* **24**, 122702 (2017).
- [8] P. Mabey, B. Albertazzi, G. Rigon, J.-R. Marquès, C. A. J. Palmer, J. Topp-Mugglestone, P. Perez-Martin, F. Kroll, F.-E. Brack, T. E. Cowan, U. Schramm, K. Falk, G. Gregori, E. Falize, and M. Koenig, Laboratory study of bilateral supernova remnants and continuous MHD shocks, *Astrophys. J.* **896**, 167 (2020).
- [9] S. Fujioka, Z. Zhang, K. Ishihara, K. Shigemori, Y. Hironaka, T. Johzaki, A. Sunahara, N. Yamamoto, H. Nakashima, T. Watanabe, H. Shiraga, H. Nishimura, and H. Azechi, Kilotesla magnetic field due to a capacitor-coil target driven by high power laser, *Sci. Rep.* **3**, 1170 (2013).
- [10] K. F. F. Law, M. B. Grandvaux, A. Morace, S. Sakata, K. Matsuo, S. Kojima, S. Lee, X. Vaisseau, Y. Arikawa, A. Yogo, K. Kondo, Z. Zhang, C. Bellei, J. J. Santos, S. Fujioka, and H. Azechi, Direct measurement of kilo-tesla level magnetic field generated with laser-driven capacitor-coil target by proton deflectometry, *Appl. Phys. Lett.* **108**, 091104 (2016).
- [11] L. Gao, H. Ji, G. Fiksel, W. Fox, M. Evans, and N. Alfonso, Ultrafast proton radiography of the magnetic fields generated by a laser-driven coil current, *Phys. Plasmas* **23**, 043106 (2016).
- [12] C. Goyon, B. B. Pollock, D. P. Turnbull, A. Hazi, L. Divol, W. A. Farmer, D. Haberberger, J. Javedani, A. J. Johnson, A. Kemp, M. C. Levy, B. Grant Logan, D. A. Mariscal, O. L. Landen, S. Patankar, J. S. Ross, A. M. Rubenchik, G. F. Swadling, G. J. Williams, S. Fujioka, K. F. F. Law, and J. D. Moody, Ultrafast probing of magnetic field growth inside a laser-driven solenoid, *Phys. Rev. E* **95**, 033208 (2017).
- [13] J. J. Santos, L. Giuffrida, S. Fujioka, Z. Zhang, P. Korneev, R. Bouillaud, S. Dorard, D. Batani, M. Chevrot, J. E. Cross, R.

- Crowston, J.-I. Dubois, J. Gazave, G. Gregori, E. Humières, S. Hulin, K. Ishihara, S. Kojima, E. Loyez, J.-r. Marquès, A. Morace, P. Nicolai, O. Peyrusse, A. Poyé, D. Raffestin, J. Ribolzi, M. Roth, G. Schaumann, F. Serres, V. T. Tikhonchuk, P. Vacar, and N. Woolsey, Laser-driven platform for generation and characterization of strong quasi-static magnetic fields, *New J. Phys.* **17**, 083051 (2015).
- [14] J. J. Santos, M. Bailly-Grandvaux, M. Ehret, A. V. Arefiev, D. Batani, F. N. Beg, A. Calisti, S. Ferri, R. Florido, P. Forestier-Colleoni, S. Fujioka, M. A. Gigosos, L. Giuffrida, L. Gremillet, J. Honrubia, S. Kojima, P. Korneev, K. F. F. Law, J. R. Marquès, A. Morace, C. Mossé, O. Peyrusse, S. Rose, M. Roth, S. Sakata, G. Schaumann, F. Suzuki-Vidal, V. T. Tikhonchuk, T. Toncian, N. Woolsey, and Z. Zhang, Laser-driven strong magnetostatic fields with applications to charged beam transport and magnetized high energy-density physics, *Phys. Plasmas* **25**, 056705 (2018).
- [15] B. J. Zhu, Y. T. Li, D. W. Yuan, Y. F. Li, F. Li, G. Q. Liao, J. R. Zhao, J. Y. Zhong, F. B. Xue, S. K. He, W. W. Wang, F. Lu, F. Q. Zhang, L. Yang, K. N. Zhou, N. Xie, W. Hong, H. G. Wei, K. Zhang, B. Han, X. X. Pei, C. Liu, Z. Zhang, W. M. Wang, J. Q. Zhu, Y. Q. Gu, Z. Q. Zhao, B. H. Zhang, G. Zhao, and J. Zhang, Strong magnetic fields generated with a simple open-ended coil irradiated by high power laser pulses, *Appl. Phys. Lett.* **107**, 261903 (2015).
- [16] X. X. Pei, J. Y. Zhong, Y. Sakawa, Z. Zhang, K. Zhang, H. G. Wei, Y. T. Li, Y. F. Li, B. J. Zhu, T. Sano, Y. Hara, S. Kondo, S. Fujioka, G. Y. Liang, F. L. Wang, and G. Zhao, Magnetic reconnection driven by Gekko XII lasers with a Helmholtz capacitor-coil target, *Phys. Plasmas* **23**, 032125 (2016).
- [17] K. Matsuo, H. Nagatomo, Z. Zhang, P. Nicolai, T. Sano, S. Sakata, S. Kojima, S. H. Lee, K. F. F. Law, Y. Arikawa, Y. Sakawa, T. Morita, Y. Kuramitsu, S. Fujioka, and H. Azechi, Magnetohydrodynamics of laser-produced high-energy-density plasma in a strong external magnetic field, *Phys. Rev. E* **95**, 053204 (2017).
- [18] H. B. Cai, S. P. Zhu, and X. T. He, Effects of the imposed magnetic field on the production and transport of relativistic electron beams, *Phys. Plasmas* **20**, 072701 (2013).
- [19] A. Arefiev, T. Toncian, and G. Fiksel, Enhanced proton acceleration in an applied longitudinal magnetic field, *New J. Phys.* **18**, 105011 (2016).
- [20] M. Bailly-Grandvaux, J. J. Santos, C. Bellei, P. Forestier-Colleoni, S. Fujioka, L. Giuffrida, J. J. Honrubia, D. Batani, R. Bouillaud, M. Chevrot, J. E. Cross, R. Crowston, S. Dorard, J. L. Dubois, M. Ehret, G. Gregori, S. Hulin, S. Kojima, E. Loyez, J. R. Marquès, A. Morace, P. Nicolai, M. Roth, S. Sakata, G. Schaumann, F. Serres, J. Serval, V. T. Tikhonchuk, N. Woolsey, and Z. Zhang, Guiding of relativistic electron beams in dense matter by longitudinally imposed strong magnetic fields, *Nat. Commun.* **9**, 102 (2018).
- [21] S. X. Luan, W. Yu, F. Y. Li, D. Wu, Z. M. Sheng, M. Y. Yu, and J. Zhang, Laser propagation in dense magnetized plasma, *Phys. Rev. E* **94**, 053207 (2016).
- [22] T. Sano, Y. Tanaka, N. Iwata, M. Hata, K. Mima, M. Murakami, and Y. Sentoku, Broadening of cyclotron resonance conditions in the relativistic interaction of an intense laser with overdense plasmas, *Phys. Rev. E* **96**, 043209 (2017).
- [23] T. Sano, M. Hata, D. Kawahito, K. Mima, and Y. Sentoku, Ultrafast wave-particle energy transfer in the collapse of standing whistler waves, *Phys. Rev. E* **100**, 053205 (2019).
- [24] L. J. Perkins, B. G. Logan, G. B. Zimmerman, and C. J. Werner, Two-dimensional simulations of thermonuclear burn in ignition-scale inertial confinement fusion targets under compressed axial magnetic fields, *Phys. Plasmas* **20**, 072708 (2013).
- [25] T. Johzaki, T. Taguchi, Y. Sentoku, A. Sunahara, H. Nagatomo, H. Sakagami, K. Mima, S. Fujioka, and H. Shiraga, Control of an electron beam using strong magnetic field for efficient core heating in fast ignition, *Nucl. Fusion* **55**, 053022 (2015).
- [26] S. Sakata, S. Lee, T. Johzaki, H. Sawada, Y. Iwasa, H. Morita, K. Matsuo, K. F. F. Law, A. Yao, M. Hata, A. Sunahara, S. Kojima, Y. Abe, H. Kishimoto, A. Syuhada, T. Shiroto, A. Morace, A. Yogo, N. Iwata, M. Nakai, H. Sakagami, T. Ozaki, K. Yamanoi, T. Norimatsu, Y. Nakata, S. Tokita, N. Miyanaga, J. Kawanaka, H. Shiraga, K. Mima, H. Nishimura, M. Bailly-Grandvaux, J. J. Santos, H. Nagatomo, H. Azechi, R. Kodama, Y. Arikawa, Y. Sentoku, and S. Fujioka, Magnetized fast isochoric laser heating for efficient creation of ultra-high-energy-density states, *Nat. Commun.* **9**, 3937 (2018).
- [27] K. Matsuo, N. Higasi, N. Iwata, S. Sakata, S. Lee, T. Johzaki, H. Sawada, Y. Iwasa, K. F. F. Law, H. Morita, Y. Ohiai, S. Kojima, Y. Abe, M. Hata, T. Sano, H. Nagatomo, A. Sunahara, A. Morace, A. Yogo, M. Nakai, H. Sakagami, T. Ozaki, K. Yamanoi, T. Norimatsu, Y. Nakata, S. Tokita, J. Kawanaka, H. Shiraga, K. Mima, H. Azechi, R. Kodama, Y. Arikawa, Y. Sentoku, and S. Fujioka, Petapascal Pressure Driven by Fast Isochoric Heating with a Multipicosecond Intense Laser Pulse, *Phys. Rev. Lett.* **124**, 035001 (2020).
- [28] V. V. Korobkin and S. Motylev, Laser method for producing strong magnetic fields, *Sov. Tech. Phys. Lett.* **5**, 474 (1979).
- [29] J. F. Seely, Pulsed megagauss fields produced by laser-driven coils, *Appl. Phys. B* **31**, 37 (1983).
- [30] H. Daido, F. Miki, K. Mima, M. Fujita, K. Sawai, H. Fujita, Y. Kitagawa, S. Nakai, and C. Yamanaka, Generation of a Strong Magnetic Field by an Intense CO₂ Laser Pulse, *Phys. Rev. Lett.* **56**, 846 (1986).
- [31] C. Courtois, A. D. Ash, D. M. Chambers, R. A. D. Grundy, and N. C. Woolsey, Creation of a uniform high magnetic-field strength environment for laser-driven experiments, *J. Appl. Phys.* **98**, 054913 (2005).
- [32] G. Fiksel, W. Fox, L. Gao, and H. Ji, A simple model for estimating a magnetic field in laser-driven coils, *Appl. Phys. Lett.* **109**, 134103 (2016).
- [33] V. T. Tikhonchuk, M. Bailly-Grandvaux, J. J. Santos, and A. Poyé, Quasistationary magnetic field generation with a laser-driven capacitor-coil assembly, *Phys. Rev. E* **96**, 023202 (2017).
- [34] P. Mora, Thin-foil expansion into a vacuum, *Phys. Rev. E* **72**, 056401 (2005).
- [35] G. J. Williams, S. Patankar, D. A. Mariscal, V. T. Tikhonchuk, J. D. Bude, C. W. Carr, C. Goyon, M. A. Norton, B. B. Pollock, A. M. Rubenchik, G. F. Swadling, E. R. Tubman, and J. D. Moody, Laser intensity scaling of the magnetic field from a laser-driven coil target, *J. Appl. Phys.* **127**, 083302 (2020).
- [36] S. C. Wilks, A. B. Langdon, T. E. Cowan, M. Roth, M. Singh, S. Hatchett, M. H. Key, D. Pennington, and R. A. Snavely, Energetic proton generation in ultra-intense laser-solid interactions, *Phys. Plasmas* **8**, 542 (2001).

- [37] Y. Sentoku, T. E. Cowan, A. Kemp, and H. Ruhl, High energy proton acceleration in interaction of short laser pulse with dense plasma target, *Phys. Plasmas* **10**, 2009 (2003).
- [38] A. B. Zylstra, C. K. Li, H. G. Rinderknecht, F. H. Séguin, R. D. Petrasso, C. Stoeckl, D. D. Meyerhofer, P. Nilson, T. C. Sangster, S. L. Paep, A. Mackinnon, and P. Patel, Using high-intensity laser-generated energetic protons to radiograph directly driven implosions *Rev. Sci. Instr.* **83**, 013511 (2012).
- [39] E. J. Tuohy, T. H. Lee, and H. P. Fullerton, Transient resistance of conductors, *IEEE Trans. Power Apparatus Syst.* **87**, 094505 (1968).
- [40] P. A. Gourdain, M. B. Adams, J. R. Davies, and C. E. Seyler, Axial magnetic field injection in magnetized liner inertial fusion, *Phys. Plasmas* **24**, 102712 (2017).
- [41] J. D. Moody, A. Johnson, J. Javedani, E. Carroll, J. Fry, B. Kozioziemski, S. O. Kucheyev, B. G. Logan, B. B. Pollock, H. Sio, D. Strozzi, W. A. Stygar, V. Tang, and S. Winters, Transient magnetic field diffusion considerations relevant to magnetically assisted indirect drive inertial confinement fusion, *Phys. Plasmas* **27**, 112711 (2020).
- [42] H. Morita, A. Sunahara, Y. Arikawa, H. Azechi and S. Fujioka, Numerical analysis of pulsed magnetic field diffusion dynamics in gold cone target, *Phys. Plasmas* **25**, 094505 (2018).
- [43] J. Clérouin, P. Noiret, P. Blottiau, V. Recoules, B. Siberchicot, P. Renaudin, C. Blancard, G. Faussurier, B. Holst and C. E. Starrett, A database for equations of state and resistivities measurements in the warm dense matter regime, *Phys. Plasmas* **19**, 082702 (2012).
- [44] V. Tikhonchuk, J. Santos, and P. Korneev (unpublished).
- [45] D. W. Forslund, J. M. Kindel, and K. Lee, Theory of Hot-Electron Spectra at High Laser Intensity, *Phys. Rev. Lett.* **39**, 284 (1977).
- [46] S. Atzeni and J. Meyer-Ter-Vehn, Thermal waves and ablative drive, *The Physics of Inertial Fusion*, (Oxford University Press Inc., 2011), Chap. 7, p. 225.